Journal of Nuclear Materials 443 (2013) 128–139

Contents lists available at SciVerse ScienceDirect

Journal of Nuclear Materials

journal homepage: www.elsevier.com/locate/jnucmat

Spatially resolved stochastic cluster dynamics for radiation damage evolution in nanostructured metals

Aaron Y. Dunn [a], Laruent Capolungo [a,*], Enrique Martinez [b], Mohammed Cherkaoui [a]

[a] George W. Woodruff School of Mechanical Engineering, Georgia Institute of Technology, UMI 2958 Georgia Tech CNRS, 57070 Metz, France
[b] Los Alamos National Laboratory, Los Alamos, NM, United States

ARTICLE INFO

Article history:
Received 12 March 2013
Accepted 3 July 2013
Available online 13 July 2013

ABSTRACT

A spatially resolved stochastic cluster dynamics (SRSCD) model is introduced to describe radiation-induced defect evolution in metals. The stochastic nature of the method allows SRSCD to model more chemical species and more mobile defects than rate theory methods without loss of computational efficiency, while reaching larger timescales and simulating larger volumes than object-oriented kinetic Monte Carlo (OKMC) methods. To comprehend the capabilities of the method and access new understanding of defect evolution, SRSCD is used in three scenarios. In the first, the results of Frenkel pair implantation are found to match those of rate theory in both spatially homogeneous and spatially resolved media. Next, to study spatial resolution effects and correspondence to OKMC, the results of 20 keV cascade implantation into copper is simulated and an acceptable match with OKMC is found. Finally the method is used to study the problem of helium desorption in thin iron foils. The model is compared with available experimental measures and is found to be in good agreement. The ability of SRSCD to include many mobile species of defects allows a detailed analysis of the mechanisms of helium release from the free surface of the iron foils. As a result new dominant mechanisms of helium release are discussed as well as their operating regimes.

1. Introduction

Polycrystalline materials that take advantage of nanometer scale properties, such as ODS steels and nano-laminates, have demonstrated radiation damage resistance beyond that of current generation nuclear materials [1,2]. However, the complex microstructure of such materials makes modeling their behavior increasingly difficult. For example, radiation damage in nano-layered metals such as Cu–Nb cannot be modeled using spatially homogeneous methods due to the dependence of their behavior on their layered geometries and high interface density [3,4]. In addition, even standard polycrystalline materials have spatial inhomogeneities in the form of grain boundaries and dislocations that affect radiation damage evolution [5–8]. However, these are treated as homogeneous sink terms in most rate theory simulations [9,10]. In order to predict the performance of next-generation materials in various reactor environments, radiation damage models must be both microstructure-dependent and extend over long spatial and temporal domains.

The two commonly used methods for simulating spatially resolved time-evolution of radiation damage in metals are the object kinetic Monte Carlo method (OKMC) [10–13] and spatially resolved rate theory methods [14–18], using finite element or finite difference algorithms for the spatial dependence. Each of these methods presents challenges due to computational demands. OKMC simulations limit the number of assumptions made about defect evolution by following individual defects as they diffuse stochastically throughout a material. However, due to the fact that the simulation follows each defect's diffusion pathway, simulations of reactor-relevant irradiation conditions can become computationally prohibitive using this method. Displacement damage in OKMC simulations is typically limited to less than 1 dpa and the minimum concentration of defects that can be simulated is limited to one defect per simulation cell volume [10]. Spatially resolved rate theory assumes spatial homogeneity within each volume element and thus does not track individual defect movements. In contrast to OKMC, rate theory simulations can reach dpa levels of 100 or more and can model arbitrarily small defect concentrations [10]. However, the number of rate equations to be solved increases exponentially with the number of species modeled [19]. Increased numbers of mobile defect species, such as glissile interstitial loops, also dramatically increases the complexity of the rate equations to be solved. The effects of impurities, alloying elements, and multi-species gas implantation on microstructural evolution have been shown to be significant [20–23], but these simulations are frequently not within the scope of feasible rate theory simulations.

An alternative approach to solving spatially homogeneous problems of this type, first proposed for any chemical species by

* Corresponding author. Tel.: +33 (0)3 87 20 39 49.
E-mail address: laurent.capolungo@me.gatech.edu (L. Capolungo).

0022-3115/$ - see front matter © 2013 Elsevier B.V. All rights reserved.
http://dx.doi.org/10.1016/j.jnucmat.2013.07.009

Gillespie [24] and developed further for radiation defects in metals by Marian and Bulatov [19], avoids many of these problems. In this approach, called stochastic cluster dynamics, the rate equations of traditional rate theory are treated in a homogeneous volume element, but the populations of defects are limited to integer populations within the volume. The reactions between defects such as clustering and dissociation are treated stochastically, using a Monte Carlo algorithm. Thus, the migration of individual defects is ignored and the simulation is able to include large numbers of mobile species which can interact without exponentially increasing computational time.

In order to modify this approach for problems in which nano- and micro-scale spatial dependence is necessary, the present work amends the method of stochastic cluster dynamics by creating several volume elements. Inside each element, the population of defects is assumed to be homogeneously distributed, but migration can occur between elements based on diffusion rates, defect concentrations, and element sizes. Gillespie [24] in fact proposes including spatial dependence in this way. Thus, free surfaces, inhomogeneous defect implantation, and other effects can be studied. This approach will be referred to as spatially resolved stochastic cluster dynamics (SRSCD).

The document is organized as follows: First, for the sake of comparison with rate theory [10] and validation, SRSCD is used to simulate the evolution of defects in a homogeneous system implanted with Frenkel pairs. This system is then modified to model a thin foil with free surfaces, and the results of SRSCD are compared to spatially resolved rate theory and shown to match. Second, in order to assess the correspondence of SRSCD with OKMC [13], implantation and evolution of 20 keV cascades in Cu is studied. The spatial resolution of the model is shown to be necessary for reasonable agreement between OKMC and SRSCD. Finally, SRSCD is used to identify the dominant mechanisms of helium desorption in thin iron foils as a function of temperature and foil thickness. Simulations are compared to available experimental data [25] and spatially resolved rate theory [15]. The ability of this simulation to include more mobile defect species than the rate theory simulation allows a more detailed analysis of the mechanism of helium release from the foil. This reveals new regimes in which the dominant mechanism for helium release changes from migration of mobile HeV_2 and He_2V_3 clusters to dissociation of interstitial helium from larger He_mV_n clusters.

2. Rate equations and SRSCD formulation

In an infinite, isotropic medium, the evolution of the defect populations can be modeled by tracking individual defect locations and behaviors, or by using a mean field approximation [10]. The use of a mean field approximation allows the simulation to ignore individual defect behavior, thus reducing the computation time, but assumes spatial homogeneity of defects. In this section, the rate equations for mean field rate theory (MFRT) are described and adapted to the model of the present work.

2.1. Rate theory background

Here we will present the rate equations for a simple MFRT model containing only two mobile species – vacancies and interstitials – and no helium. This model is taken from Stoller et al. [10]. The evolution of the atomic fraction of SIA (i) or vacancy (v) clusters size n is given by:

$$\begin{aligned}\frac{dC_{vn}}{dt} &= K_{vn}(t) + J_v(n-1,t) - J_v(n,t)\\ \frac{dC_{in}}{dt} &= K_{in}(t) + J_i(n-1,t) - J_i(n,t)\end{aligned} \tag{1}$$

where K_{vn} and K_{in} are the generation rate of vacancy and self-interstitial clusters of size n, $J_v(n-1,t)$ and $J_i(n-1,t)$ are the rate of vacancy and interstitial clusters of size $n-1$ converting to size n, and $J_v(n,t)$ and $J_i(n,t)$ are the rate of vacancy and interstitial clusters of size n converting to size $n+1$. Care should be taken here to note that $C_{vn}(t)$ and $C_{in}(t)$ are atomic fractions, which are unitless. Other formulations of MFRT use concentration formulated in defects per volume, and constants are adjusted accordingly [14,19]. In a simple model with only Frenkel pair implantation and no migration of clusters, $K_n = 0$ for all n except $n = 1$. The reactions that are accounted for in the growth and annihilation of vacancy and interstitial clusters are as follows:

1. $V_n + V \rightarrow V_{n+1}$ and $I_n + I \rightarrow I_{n+1}$ cluster growth
2. $V_n \rightarrow V_{n-1} + V$ and $I_n \rightarrow I_{n-1} + I$ thermally activated cluster dissociation
3. $V_n + I \rightarrow V_{n-1}$ and $I_n + V \rightarrow I_{n-1}$ vacancy-interstitial annihilation

Taking these reactions into account, the cluster growth terms in Eq. (1) are expressed as

$$\begin{aligned}J_v(n,t) &= P_{vn}(t)C_{vn}(t) - Q_{v(n+1)}(t)C_{v(n+1)}(t)\\ J_i(n,t) &= P_{in}(t)C_{in}(t) - Q_{i(n+1)}(t)C_{i(n+1)}(t)\end{aligned} \tag{2}$$

where P_{vn} and P_{in} are the rates of $V_n + V$ and $I_n + I$ clustering respectively, and Q_{vn} and Q_{in} are the rates of recombination and dissociation of vacancy and interstitial clusters of size n. Assuming thermally activated, 3D diffusion, spherical vacancy clusters, and interstitial clusters in the form of circular dislocation loops, the clustering and dissociation rates are given by [10,26]:

$$\begin{aligned}P_{vn}(t) &= \omega n^{1/3} D_v C_v(t)\\ P_{in}(t) &= Z_{\mathrm{int}}\omega_{2D} n^{1/2} D_i C_i(t)\\ Q_{vn}(t) &= Q^i_{vn} + Q^v_{vn} = \omega n^{1/3}\left(D_i C_i(t) + D_v e^{-\frac{E_b^v(n)}{k_b T}}\right)\\ Q_{in}(t) &= Q^v_{in} + Q^i_{in} = \omega_{2D} n^{1/2}\left(D_v C_v(t) + D_i e^{-\frac{E_b^i(n)}{k_b T}}\right)\end{aligned} \tag{3}$$

Here, $C_{v,i}$ and $D_{v,i}$ are the concentration and diffusion rates of free vacancies and interstitials, respectively. Z_{int} is a constant reflecting the preference of interstitial clusters to absorb other interstitials, commonly taken as $Z_{\mathrm{int}} = 1.15$. $E_b^{v,i}(n)$ is the binding energy of a vacancy or interstitial to a cluster size $n-1$, k_b is Boltzmann's constant, and T is the temperature. The constants ω and ω_{2D} are geometric constants determined by the sink strength of spherical and circular absorbers [9,10],

$$\begin{aligned}\omega &= \left(\frac{48\pi^2}{\Omega^2}\right)^{1/3}\\ \omega_{2D} &= \left(\frac{4\pi}{\Omega b}\right)^{1/2}\end{aligned} \tag{4}$$

where Ω is an atomic volume and b is the Burgers vector of a dislocation loop.

The rate equations for the time evolution of mobile point defects are more complicated due to the large number of available interactions. The rate equations for single vacancies and single interstitials are as follows [10]:

$$\begin{aligned}\frac{dC_v}{dt} &= K_v - \mu_R(D_i + D_v)C_i(t)C_v(t)\\ &\quad - \sum_{n=2}^{\infty}\left[P_{vn}(t)C_{vn}(t) + Q^v_{in}(t)C_{in}(t) - Q^v_{vn}(t)C_{vn}(t)\right]\\ &\quad - 2P_{v1}(t)C_v(t) + Q^v_{v2}(t)C_{v2}(t)\end{aligned}$$

$$\frac{dC_i}{dt} = K_i - \mu_R(D_i + D_v)C_i(t)C_v(t) - \sum_{n=2}^{\infty}\left[P_{in}(t)C_{in}(t) + Q^i_{vn}(t)C_{vn}(t) - Q^i_{in}(t)C_{in}(t)\right] - 2P_{i1}(t)C_i(t) + Q^i_{i2}(t)C_{i2}(t) \quad (5)$$

where μ_R is a coefficient for the recombination of point defects, given by $\mu_R = \frac{4\pi(r_v+r_i)}{\Omega}$. The final terms in each expression represent the fact that the reactions $v + v \Leftrightarrow 2v$ and $i + i \Leftrightarrow 2i$ add or remove two point defects for each reaction.

Rate equations can vary widely based on the number of defect types present in the system, which defect types are allowed to migrate, and the allowed reactions of the model chosen. As noted by others [19], the number of rate equations required increases exponentially with the number of defect species due to the need to simulate mixed-species clusters. The complexity of the equations also increases as the number of migrating defects of a given species increases. Although grouping schemes exist in rate theory for large clusters in order to speed computation [27], rate theory simulations are commonly limited to a small number of species and mobile defects.

2.2. Reaction rates

In the following sections, it will become useful to discuss the reaction rate of a specific reaction, for example $v + 3v \rightarrow 4v$, instead of the entire rate equation governing the population of a single defect type. It can be seen from above that the rate of combination of a mobile point defect i and a sink is given by

$$\textit{reaction rate} = k^2 D_i C_i(t) \quad (6)$$

where the sink strength k^2 has units $\frac{1}{m^2}$ and represents the inverse of the square of the mean free path travelled by the point defect before it is absorbed by the stationary defect. It can be seen that the above equations are expressed in this form, with k^2 depending on many factors, including the size and shape of the sinks, whether the sink is also migrating, and the type of migration (1D vs 3D).

When many sink types are present in a system, sink strengths are not independent and have been shown to increase when other sinks are present in high concentrations [28]. This effect is most likely to be significant in the sink strengths of grain boundaries and free surfaces due to the large number of defects within the grains or metal layers. Large planar sinks therefore should not be treated as homogeneously distributed sinks with constant sink strength k^2.

In this simulation, planar sinks act as 'primary' sinks. These sinks are simulated using boundary conditions on the system by setting the concentration of all defect types equal to 0 at a free surface or perfectly absorbing grain boundary. All other defects (helium, vacancies, and self-interstitials and their clusters) are simulated as homogeneously distributed 'secondary' sinks with sink strength k^2. This approach has been used in other simulations of sink strength and defect evolution in metals [17,28,29].

2.2.1. 3D-migrating defects

To calculate the sink strength of defects and defect clusters, it will first be useful to note that for a spherical cluster size n, the radius is given by

$$r = \left(\frac{3n\Omega}{4\pi}\right)^{1/3} \quad (7)$$

and for a circular interstitial dislocation loop size n, the radius is given by

$$r = \left(\frac{n\Omega}{\pi b}\right)^{1/2} \quad (8)$$

where Ω is the atomic volume and b is the Burgers vector.

For a point defect migrating in three dimensions interacting with a spherical (immobile) sink j, the sink strength is given by [9]:

$$k^2 = \frac{4\pi r_j C_j}{\Omega} \quad (9)$$

Thus, the reaction rate for a point defect to interact with a spherical sink is

$$\textit{reaction rate} = \omega n_j^{1/3} D_i C_i C_j \quad (10)$$

For a point defect interacting with a circular (immobile) sink j, the sink strength is given by [10]:

$$k^2 = \frac{2\pi r_j C_j}{\Omega} \quad (11)$$

Thus, the reaction rate for a point defect to interact with a circular sink is

$$\textit{reaction rate} = \omega_{2D} n_j^{1/2} D_i C_i C_j \quad (12)$$

The reaction rates presented above correspond to the clustering terms in the rate equations presented in the previous section.

In the previous equations, interstitial clusters are treated as circular dislocation loops, and their cross-section for interaction with migrating point defects is adjusted accordingly. However, these defects are assumed to be immobile in most rate theory simulations. By contrast, atomistics studies have shown that the small dislocation loops formed by self-interstitial clusters are in fact very mobile, undergoing one-dimensional glide motion with migration energy less than 0.1 eV [11,30]. The following rate equations will account for interactions of multiple mobile defects of varying geometry and migration dimensionality.

The first modification of Eqs. (10) and (12) occurs when the point defect and the sink are both mobile, spherical defects. In that case, the interaction radius becomes the sum of the two radii of the spherical objects, and the relative diffusion rate is the sum of the two diffusion rates of each defect. This is the same as the sum of the rate at which mobile defect i encounters stationary defect j and mobile defect j encounters stationary defect i. Thus the reaction rate for two spherical defects interacting is

$$\textit{reaction rate} = \omega\left(n_i^{1/3} + n_j^{1/3}\right)(D_i + D_j)C_i(t)C_j(t) \quad (13)$$

2.2.2. 1D-migrating defects

Next, we will treat the case of migrating circular dislocation loops. Since these loops migrate in one dimension, their cross-section for interaction with other defects is different than the case of 3D diffusion. For the case of a point defect migrating in 1D interacting with stationary spherical sinks with absorption cross section σ, the inverse of the average distance travelled before being trapped at a sink is given by [31]:

$$\frac{1}{\lambda} = c\sigma = \frac{C\sigma}{\Omega} \quad (14)$$

where the volume concentration of sinks c has been changed to the atomic concentration divided by atomic volume $\frac{C}{\Omega}$. Using $\sigma = \pi r^2$ for the absorption cross section of a spherical sink, the sink strength $k^2 = \frac{1}{\lambda^2}$ is given by [32]:

$$k^2 = \left(\frac{\pi r^2 C}{\Omega}\right)^2 \quad (15)$$

We next consider a circular dislocation loop i migrating and interacting with an (immobile) point defect sink j. The interaction radius used here is the radius of the circular dislocation loop. Substituting Eq. (8) into Eq. (15), the reaction rate becomes:

$$\text{reaction rate} = \left(\frac{n_i}{b}\right)^2 D_i C_i(t) C_j(t)^2 \tag{16}$$

Note that the reaction rate is quadratic in concentration of the sinks. The fact that we are using the radius of a circular object in the formula for sink strength of a spherical object means that our reaction rate is an upper estimate for the reaction radius of this reaction. However, the form of the reaction rate should remain the same and only vary by a constant due to the shape of the defects involved.

The reaction rate for a circular dislocation loop i interacting with a sessile spherical cluster j is given by the same formula, using the reaction radius as the sum of the radii of the circular loop and the spherical cluster. This reaction rate is given by

$$\text{reaction rate} = \left[\left(\frac{n_i}{b}\right)^{1/2} + \left(\frac{9\pi n_j^2}{16\Omega}\right)^{1/6}\right]^4 D_i C_i(t) C_j(t)^2 \tag{17}$$

Note that the form of this reaction is the same as Eq. (16), with only a change in the radius term accounting for the size of the spherical cluster.

If both the circular dislocation loop i and the spherical defect j migrate, one in 1D and the other in 3D, the reaction rate becomes the sum of the reaction rates for the two types of migration. In this case, we take the sum of the rate for a 1D migrating circular loop to react with a sessile spherical cluster and the rate for a 3D migrating spherical cluster to react with a sessile loop. Thus the reaction rate becomes:

$$\begin{aligned}\text{reaction rate} = &\left[\left(\frac{n_i}{b}\right)^{1/2} + \left(\frac{9\pi n_j^2}{16\Omega}\right)^{1/6}\right]^4 D_i C_i(t) C_j(t)^2 \\ &+ \left(\omega_{2D} n_i^{1/2} + \omega n_j^{1/3}\right) D_j C_i(t) C_j(t)\end{aligned} \tag{18}$$

Here, the first term accounts for the migration of the dislocation loop and the second term accounts for the migration of the spherical defect. Both terms use the sum of the radii of the dislocation loop and the spherical defect as the reaction radius.

Finally, the reaction rate for two 1D-migrating dislocation loops to interact is again found by summing the rates for each individual loop interacting with the other while the other is stationary. Again, the radius used in the reaction is the sum of the radii of the two loops. Thus, the reaction rate for two 1D-migrating dislocation loops i and j to combine is given by:

$$\text{reaction rate} = \frac{\left(n_i^{1/2} + n_j^{1/2}\right)^4}{b^2} \left(D_i C_j(t) + D_j C_i(t)\right) \times C_i(t) C_j(t) \tag{19}$$

2.2.3. Mixed 3D–1D migration

Small SIA clusters have been found to migrate in one dimension along close-packed directions but with occasional changes between equivalent close-packed directions [11]. Direction changes occur according to an Arrhenius law such that the migration behavior transitions between one-dimensional at low temperatures and three-dimensional at higher temperatures. Assuming 1D and 3D sink strengths are known, the sink strength due to a given sink type i for a defect migrating with this mixed 1D–3D character has been derived by Trinkaus et al. [33]:

$$k_i^2 = \frac{k_{i(1D)}^2}{2}\left(1 + \left(1 + \frac{4}{\frac{l^2 k_{1D}^2}{12} + \frac{k_{i(1D)}^4}{k_{i(3D)}^4}}\right)^{1/2}\right) \tag{20}$$

where k_{1D}^2 is the total sink strength for all sinks using 1D migration, $k_{i(1D)}^2$ and $k_{i(3D)}^2$ are the 1D and 3D sink strengths of sink i, and l is the average distance travelled in one dimension before a direction change.

It was verified in this work that the sink strength calculated in this way reproduces the 3D sink strength in the limit of frequent direction changes and sparse sinks and reproduces the 1D sink strength in the limit of infrequent direction changes. In this work, sink strengths calculated in this way are only used in the simulations of helium desorption from thin iron films, as discussed in later sections.

2.3. Reaction rates for discrete elements

The central idea of stochastic rate theory is to solve these rate equations stochastically in a finite volume element. Given a volume element with volume V, if the concentration of defects in the volume is C (in atomic fraction), then the total number of defects in that volume is $N = \frac{CV}{\Omega}$. This number is an integer value, and reaction rates for defects not present in the volume are not calculated.

Given an initial set of defects within a volume element, assuming spatial homogeneity within that element, the reaction rates for any two defects to combine or any one defect to dissociate are given by the same reaction rates as above, which are converted to rates for a finite volume element by multiplying them by $\frac{V}{\Omega}$:

$$\left(\frac{dC}{dt}\right)\left(\frac{V}{\Omega}\right) = \frac{dN}{dt} \tag{21}$$

Converting concentration C into $\frac{N\Omega}{V}$ and multiplying all reaction rates by $\frac{V}{\Omega}$, we convert all reaction rates to finite-volume rates with units s^{-1}. Table 1 shows these rates. It should be noted that other formulations of stochastic rate theory [19] have used concentration rate equations that are in units of defects/m^3, so these equations are only multiplied by V.

2.4. Spatially resolved rate equations

So far, reaction rates have been derived for a single finite volume element which is assumed to be spatially homogeneous throughout. This is an approximation of an infinite medium. However, a physically representative prediction of defect evolution in a heterogeneous microstructure, e.g. polycrystals, nano-structured materials, and nano-laminates, can only be accessed through a spatially resolved method. Indeed, the behavior of defects in the neighborhood of grain boundaries, dislocations, and hetero-interfaces is known to be different from the bulk [4–8,17,34–36]. While traditional approaches use averaging arguments to treat the impact of grain boundaries and dislocations in homogeneous models, it is likely that in nano-structured materials this approximation can no longer be made. In addition, defect populations resulting from cascade implantation have been shown to depend on the spatial resolution of the initial cascade state [11,13,14]. It is therefore necessary to develop a method that can simulate both large timescales and the spatially resolved structures of nano-structured materials.

It was noted by the original author of stochastic rate theory [24] that the system could approximate spatial resolution by creating several volume elements instead of a single one. Within each volume element, the system is assumed to be 'well-mixed' and therefore spatially homogeneous, but differences in numbers of defects occur between elements. The reaction rates of combination and dissociation are calculated within each element according to the rate equations presented above. To calculate the reaction rates of migration between elements, we begin with a standard gradient-driven diffusion equation (in units of atomic fraction):

Table 1
Reaction rates for vacancy and interstitial reactions in a finite volume element, size V. N_i indicates the absolute number of species i present in the volume. All rates are in units of s^{-1}. 3D SIA indicates that the SIA cluster is approximated as a sphere that migrates in three dimensions, 1D SIA indicates that the SIA cluster is approximated as a circular dislocation loop that migrates in one dimension. In the migration reaction, species X migrates from volume element i to j, with boundary surface area A_{ij} and separation L_{ij}.

Reaction	Reaction rate (s^{-1})
Clustering reactions	
$V_n + V_m \rightarrow V_{n+m}$	$\omega(n^{1/3}+m^{1/3})(D_{Vn}+D_{Vm})N_{Vn}(t)N_{Vm}(t)\frac{\Omega}{V}$
$V_n + I_m \rightarrow V_{n-m}$ or I_{m-n} (3D SIA)	$\omega(n^{1/3}+m^{1/3})(D_{Vn}+D_{Im})N_{Vn}(t)N_{Im}(t)\frac{\Omega}{V}$
$V_n + I_m \rightarrow V_{n-m}$ or I_{m-n} (1D SIA)	$\left[\left(\frac{m}{b}\right)^{1/2}+\left(\frac{9\pi n^2}{16\Omega}\right)^{1/6}\right]^4 D_{Im}N_{Im}(t)N_{Vn}(t)^2\frac{\Omega^2}{V^2}$ $+(\omega_{2D}m^{1/2}+\omega n^{1/3})D_{Vn}N_{Im}(t)N_{Vn}(t)\frac{\Omega}{V}$
$I_n + I_m \rightarrow I_{n+m}$ (3D + 3D SIA)	$Z_{\text{int}}\omega(n^{1/3}+m^{1/3})(D_{In}+D_{Im})N_{In}(t)N_{Im}(t)\frac{\Omega}{V}$
$I_n + I_m \rightarrow I_{n+m}$ (3D + 1D SIA)	$Z_{\text{int}}^4\left[\left(\frac{m}{b}\right)^{1/2}+\left(\frac{9\pi n^2}{16\Omega}\right)^{1/6}\right]^4 D_{Im}N_{Im}(t)N_{In}(t)^2\frac{\Omega^2}{V^2}$ $+(\omega_{2D}m^{1/2}+\omega n^{1/3})D_{In}N_{Im}(t)N_{In}(t)\frac{\Omega}{V}$
$I_n + I_m \rightarrow I_{n+m}$ (1D + 1D SIA)	$Z_{\text{int}}^4\frac{(n^{1/2}+m^{1/2})^4}{b^2}(D_{In}N_{Im}(t)+D_{Im}N_{In}(t))N_{In}(t)N_{Im}(t)\frac{\Omega^2}{V^2}$
Dissociation reactions	
$V_n \rightarrow V + V_{n-1}$	$\omega n^{1/3}D_V e^{-\frac{E_b(n)}{k_bT}}N_{Vn}(t)$
$I_n \rightarrow I + I_{n-1}$ (3D SIA)	$\omega n^{1/3}D_I e^{-\frac{E_b(n)}{k_bT}}N_{In}(t)$
$I_n \rightarrow I + I_{n-1}$ (1D SIA)	$\omega_{2D}n^{1/2}D_I e^{-\frac{E_b(n)}{k_bT}}N_{In}(t)$
Migration reactions	
$X^i \rightarrow X^j$ (cell i to cell j)	$D_X A_{ij}\frac{N_X^i(t)-N_X^j(t)}{VL_{ij}}$
Implantation reactions	
$0 \rightarrow V + I$	(dpa rate)$\left(\frac{V}{\Omega}\right)$
$0 \rightarrow$ (*cascade*)	$\left(\frac{\text{dpa rate}}{N_{\text{displaced}}}\right)\left(\frac{V}{\Omega}\right)$

$$\frac{dC}{dt} = \nabla\cdot(D\cdot\nabla C) + f(x,t) \tag{22}$$

where $f(x,t)$ accounts for all of the terms discussed in the previous sections.

To convert this equation to a reaction rate for a finite volume, we first integrate over the volume element and apply the divergence theorem. Neglecting $f(x,t)$, this gives:

$$\int_V \frac{dC}{dt}dV = -\oint_S (D\cdot\nabla C)\cdot\vec{n}dS \tag{23}$$

where the second integral is now a surface integral over the boundary of the element. Multiplying by $\frac{1}{\Omega}$, the left hand side of Eq. (23) is now $\frac{dN}{dt}$ where N is the absolute number of defects of this type in the volume element. We will refer to this element as i and its neighbors as j, with $j \in [1,6]$. Assuming the element is rectangular, diffusion is isotropic and constant, and approximating ∇C using the neighboring volume elements, we approximate the surface integral and get:

$$\frac{dN_i}{dt} = \sum_{\text{neighbors}}\left(\frac{DA_{ij}(N_j - N_i)}{VL_{ij}}\right) \tag{24}$$

where A_{ij} is the area of the facet connecting elements i and j and L_{ij} is the distance between the centers of the two elements. Thus the reaction rate for a defect migrating from element i to element j is given by

$$\textit{reaction rate} = DA_{ij}\frac{N_i - N_j}{VL_{ij}} \tag{25}$$

This reaction is treated similar to all other reactions listed above, with a rate (in units of s^{-1}) for a single defect to migrate from volume element i to j. This approach mirrors that of a finite-element or finite-difference approximation for spatial resolution of mean field rate theory equations, which has been carried out for some systems [14,15,17,18]. The reaction rate associated with inter-element diffusion is included in Table 1.

Using spatially resolved finite volumes in this way, materials such as thin films with free surfaces can be approximated by holding the concentration of defects outside the material equal to zero at the boundaries on one axis and applying periodic boundary conditions on other axes. Cascade implantation can also be simulated by implanting all cascade products into one volume element. The optimal method for representing cascade damage in this scheme is still an open question, since cascades are not spatially homogeneous and the local density of defects in a cascade is very high.

2.5. Monte Carlo algorithm

In order to solve the rate equations presented here in a stochastic way, reactions are chosen and time is iterated in a stochastic manner, instead of using a standard finite-difference time iteration formulation as in the case of rate theory. It has been proven [24] that this approach correctly solves the master equation for the time evolution of the entire system.

Given an initial set of defects in the system, all possible reactions and their rates can be calculated using the rates in Table 1. Thus, unlike mean field rate theory, only reaction rates for defects present in the system are calculated and only integer numbers of defects are treated. Each reaction μ has a reaction rate a_μ in the system. Therefore, the total reaction rate for the system (in reactions per second) for all reactions is

$$a = \sum_\mu a_\mu \tag{26}$$

Thus, as in standard Monte Carlo techniques, the probability that the first reaction after time t in the system will occur between time $t+\tau$ and $t+\tau+\delta\tau$ is given by

$$P_1(\tau)\delta\tau = ae^{-a\tau}\delta\tau \tag{27}$$

and the probability that the next reaction will be reaction μ is

$$P_2(\mu) = \frac{a_\mu}{a} \tag{28}$$

Therefore, in the simulation, the amount of time that passes before the next reaction is carried out is chosen stochastically by choosing a random number $r_1 \in (0,1)$ and iterating time by timestep

$$\tau = \frac{1}{a}\ln\left(\frac{1}{r_1}\right) \tag{29}$$

and reaction μ is carried out, with μ chosen by choosing a second random number $r_2 \in (0,1)$ and finding μ such that

$$\sum_{\nu=1}^{\mu-1} a_\nu < r_2 a < \sum_{\nu=1}^{\mu} a_\nu \tag{30}$$

A derivation of this algorithm can be found in [24]. After each timestep, the number of defects in the cell is updated for each defect type involved in the reaction chosen. The reaction rates for all relevant reactions are subsequently updated. Thus, if a defect type disappears from the cell during a reaction, all reaction rates associated with that defect type are removed from the list of possible reactions that the system can choose. This greatly reduces the amount of computation required compared to mean field rate theory, and allows arbitrarily sized defects to migrate without creating rate equations that are unmanageable.

Due to the spatial resolution of the system, rates for reactions are calculated within each cell and between each adjacent cell for migration reactions. However, the time iteration is carried out

for the entire system at once. Thus, only one possible reaction is chosen from among all volume elements in the system per timestep.

3. Comparison with rate theory: Frenkel pair implantation

Validation of the SRSCD model described above has been carried out through a series of simulations comparing the results of this model with those of others. The first model chosen for comparison with SRSCD is that of Stoller et al. [10] which compares the results of MFRT with OKMC. In order to simplify the rate equations used, this model treats only single vacancies and single interstitials as mobile. Circular SIA clusters are immobile in this model, so all migration is in 3D and only the corresponding reaction rates with 3D migration are used (see Table 1). In this simulation, Frenkel pairs are implanted homogeneously in an infinite, initially defect-free medium at a constant rate. The vacancy and vacancy cluster populations are recorded as a function of dpa.

To further validate the results of SRSCD, the simulation was carried out in this work using both SRSCD and MFRT to verify that the rate equations and constants were being applied correctly. The diffusion and binding parameters for this simulation are shown in Table 2. The concentration of vacancies and vacancy clusters was plotted as a function of dpa and compared to the results of Stoller et al. [10]. Note that spatial resolution was disregarded in the SRSCD model in this simulation due to the spatial homogeneity of the problem. The results of these simulations are shown in Fig. 1.

It can be seen that all three sets of results are in good agreement. Due to the fact that the MFRT and SRSCD results carried out in this work agree, any differences between these results and the results of Stoller et al. are assumed to be minor. The details of matching these results to the published results of Stoller et al. were considered out of the scope of this work and were not pursued further.

In this simulation and all SRSCD simulations presented in this article, error bars represent simple standard deviations of the result. The variation of the result between simulations depends on the total volume simulated, so standard deviation should not be interpreted as a physical result here. The choice of simulation volume was made in each case to balance computational time with precision of results.

It should also be noted that the rate theory results carried out in this study were not extended beyond 10^{-3} dpa, because of computational limitations. The stochastic method, due to its increased computational efficiency, was able to easily reach the larger 10^{-2} dpa range.

Demonstration of the spatially resolved capabilities of the SRSCD model developed here was carried out by modifying the simulation from an infinite medium to a single-crystal layer of material with thickness 400 nm and free surfaces on either side. The free surfaces are treated as infinite sinks for all migrating defects, so that any defect that migrates out of the free surface is lost from the system. This spatially-resolved system was evolved to a much smaller dpa of 10^{-6} due to computational limitations of MFRT. The spatial resolution in the rate theory model was carried out through the use of a finite difference approximation, and in the SRSCD model through the use of the method described above. The spatially resolved profiles of self-interstitial and vacancy concentrations are shown in Fig. 2.

It can be seen that the results of SRSCD and spatially resolved rate theory agree. Again, the ability of the rate theory results to reach large dpa and timescales was severely limited by the need for small enough timesteps for the solution to converge. However, since SRSCD chooses timesteps and does not compute rates for cluster populations that are not present in the material, this method could easily reach much larger dpa ranges.

Table 2
Material and experimental parameters used in the simulation of Stoller et al. [10]. Interstitials were assumed perfectly bound to interstitial clusters and could not dissociate.

Parameters used		
Temperature	373 K	
Atomic volume	1.189×10^{-2} nm^3	
Burgers vector	0.2876 nm	
dpa Rate	4×10^{-7} dpa/s	
Diffusion and binding parameters		
v Formation energy	E_f^v	1.6 eV
v Diffusion prefactor	D_0^v	6.02×10^{10} nm^2/s
v Migration energy	E_m^v	.65 eV
v_n Binding energy	$E_b^v(n)$	$E_f^v + (.2 - E_f^v)\left(\frac{n^{2/3}-(n-1)^{2/3}}{2^{2/3}-1}\right)$
i Diffusion prefactor	D_0^i	6.02×10^{10} nm^2/s
i Migration energy	E_m^i	.3 eV

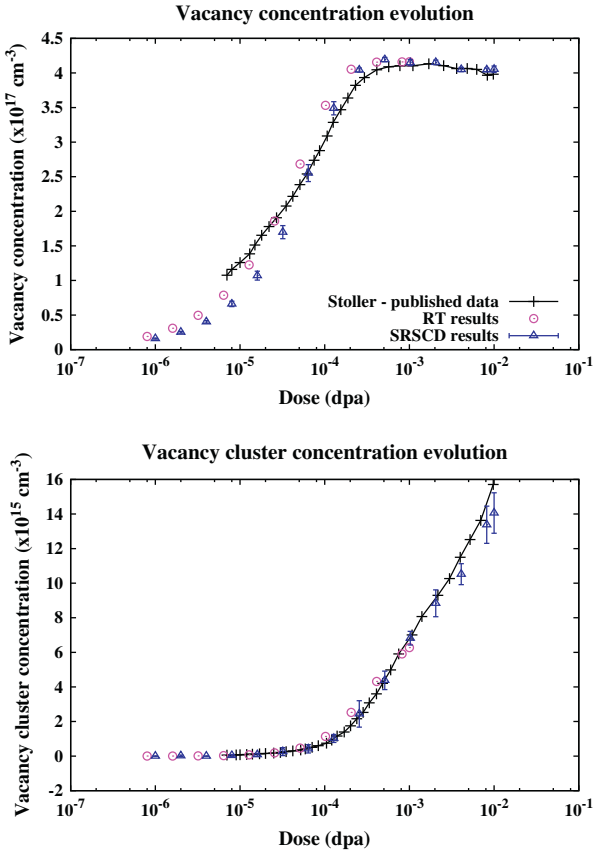

Fig. 1. Vacancy and vacancy cluster concentrations as a function of dpa for the work of Stoller et al. [10], rate theory carried out in this work, and SRSCD.

4. Comparison with kinetic Monte Carlo: Cascade implantation in Cu

One of the main benefits of SRSCD is the ability to allow many species to migrate and cluster, instead of limiting the number of mobile species as in rate theory. Object-oriented kinetic Monte Carlo simulations also have the ability to take into account the migration of larger defects and one-dimensional migration, and thus the performance of SRSCD compared to OKMC is of interest,

since SRSCD is significantly faster but necessitates more approximations.

To compare the performance of this method to OKMC, the results of cascade implantation in Cu were compared to those of Caturla et al. [13]. In these simulations, 20 keV cascades from a database produced using molecular dynamics simulations are implanted into copper at 10^{-4}dpa/s. Unlike the simulations described in the previous section, vacancy clusters up to size 4 and SIA clusters up to size 60 are mobile, with large self-interstitial clusters migrating in one dimension. Additionally, implanted cascades have spatial distributions that impact the clustering properties of the defects produced in the cascades. This is important early in the annealing of a given cascade, as the spatial orientation of the cascades impacts the subsequent time evolution of the system.

The simulation parameters are listed in Table 3. All simulation parameters used in this work are the same as reported by Caturla et al. [13]. Migration energies of vacancy clusters are taken Sabochick and Yip [37], single-interstitials from Corbett et al. [38], and small SIA clusters from Schober and Zeller [39]. Larger interstitial clusters are assumed to maintain the same migration energy but decrease their prefactor as the size of the cluster grows. The binding energy of vacancy clusters is found by fitting the values for small vacancy clusters from Sabochick and Yip [37] to a fitting function, using the formation energy of a vacancy as the binding energy of an infinite sized cluster. The binding energy of small SIA clusters is taken from Schober and Zeller [39], while the binding energy of larger SIA clusters is assumed to be the formation plus migration energy of a single SIA.

In accordance with Caturla et al., interstitial clusters of size $n = 1 - 4$ are treated as spherical defects that migrate in 3D, while larger interstitial clusters are treated as circular dislocation loops that migrate in 1D. This dimensionality applies only to the reaction rates between defects and not the actual migration between volume elements in the simulation. In this case, only 3D migration can be considered. Since FCC and BCC metals have 6 and 4 options for close-packed migration directions ($\langle 1\,1\,0\rangle$ and $\langle 1\,1\,1\rangle$ respectively) but only 3 independent axes for migration directions exist, migration between volume elements cannot be restricted such that each face of a volume element permits only one direction of migration. True one-dimensional migration could be achieved in a simple cubic crystal, which has close-packed directions in the $\langle 1\,0\,0\rangle$ directions, but this is not within the scope of this work.

The limitation of long-range migration to 3D is a main limitation of the SRSCD model compared to OKMC. The effect of this limitation is expected to be more strongly felt in systems that are spatially anisotropic, such as thin films, than systems that are spatially homogeneous over large distances such as the simulation of Caturla et al. In the latter case, the reaction rates between defects are more important than whether defects migrate from one cell to another in a given direction because the overall arrangement of defects is homogeneous.

In the simulation of Caturla et al., the effect of grain boundaries on stopping the long-range migration of fast-moving SIA clusters is accounted for by removing 1D-migrating SIA clusters that migrate a distance greater than 1 μm from the simulation cell [13]. To match this in the SRSCD simulation, interstitial clusters that migrate from one cell to another are removed from the system with a probability given by the ratio of the volume element size to the grain size. The results are weakly dependent on the grain size chosen.

This approximation for the effects of grain boundaries was tested by comparison with two other models of grain boundary behavior. In the first model, all defect types can be removed from the system when migrating from one volume element to another, instead of only 1D-migrating SIA clusters. Allowing the simulation to remove all defect types in this way did not significantly change the results, due to the fact that the vast majority of defect

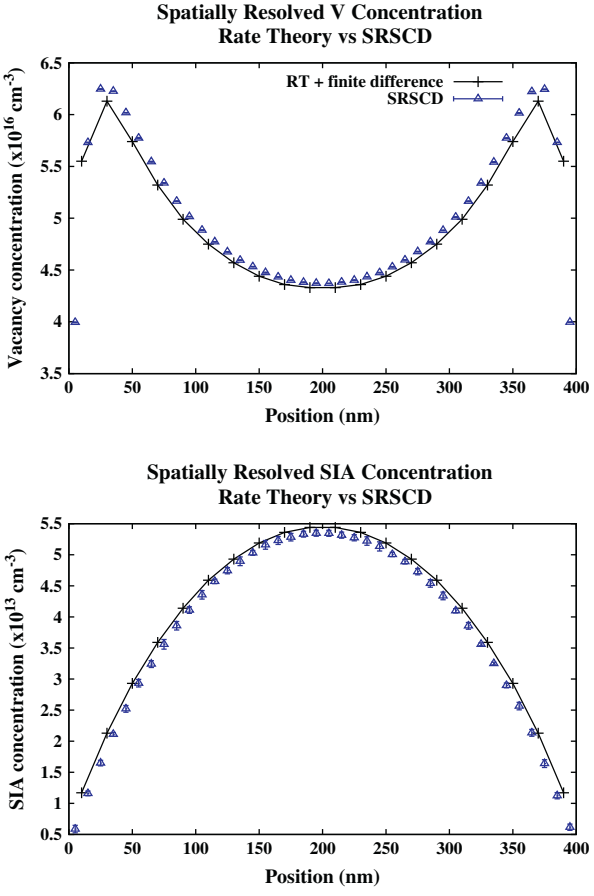

Fig. 2. Spatially resolved vacancy and interstitial concentration profiles at 10^{-6} dpa.

Table 3
Material and experimental constants used in the simulation of Caturla et al. [13] for Cu.

Parameters used	
Temperature	340 K
Atomic volume	1.17×10^{-2} nm^3
Burgers vector	.36 nm
dpa Rate	1×10^{-4} dpa/s
Grain size	1 μm
Diffusion rates	$D = D_0 e^{-\frac{E_m}{k_b T}}$
Single vacancy	E_m = .72 eV, $D_0 = 2.5 \times 10^{13}$ nm^2/s
2-*v* Cluster	E_m = .55 eV, D_0 = 3.6×10^{13} nm^2/s
3-*v* Cluster	E_m = .56 eV, $D_0 = 1.2 \times 10^{13}$ nm^2/s
4-*v* Cluster	E_m = .38 eV, $D_0 = 1.4 \times 10^{13}$ nm^2/s
Larger vacancy cluster ($n > 4$)	(immobile)
Single interstitial	E_m = .13 eV, D_0 = 2×10^{11} nm^2/s
2-*i* Cluster	E_m = .11 eV, $D_0 = 1 \times 10^{11}$ nm^2/s
3-*i* Cluster	E_m = .2 eV, $D_0 = 6.6 \times 10^{10}$ nm^2/s
4-*i* Cluster	E_m = .1 eV, $D_0 = 5 \times 10^{10}$ nm^2/s
Larger interstitial cluster ($n > 4$)	E_m = .1 eV, $D_0 = \frac{2\times10^{11}}{n}$ nm^2/s
Binding energies	
2-*v* Cluster	$E_b^v(2) = .05$ eV
3-*v* Cluster	$E_b^v(3) = .15$ eV
4-*v* Cluster	$E_b^v(4) = .28$ eV
5-*v* Cluster	$E_b^v(5) = .65$ eV
Larger vacancy cluster ($n > 5$)	$E_b^v(n) = 1.2 - 2.121(n^{2/3} - (n-1)^{2/3})$ eV
Small interstitial cluster	$E_b^i(2-4) = 1.16$ eV
Larger interstitial cluster ($n > 4$)	$E_b^i(n) = 2.62$ eV

migration is in the form of 1D-migrating SIA clusters. In the second model, the grain boundary was simulated by placing free surfaces 1 μm apart (assuming the grain boundary acts as an infinite absorber), which trapped all incident defects. Using free surfaces to simulate a grain boundary decreased the concentration of vacancy clusters slightly compared to the results obtained by simply removing the defects from the system, but the results remained similar. The results reported here represent the grain boundary model in which 1D-migrating SIA clusters are removed from the system as described above in order to match most closely the parameters of Caturla et al.

Glissile dislocation loops of SIAs with unequal Burgers vectors can interact to form immobile clusters or larger glissile dislocation loops, depending on the temperature and the geometry of the interaction [40]. In order to reproduce the simulation parameters of Caturla et al., this simulation assumes that if two dislocation loops of SIAs cluster they are assumed to form a junction and thus become immobile. These immobile interstitial clusters remain in the system and can act as sinks for other defects but cannot migrate.

In order to reproduce this simulation using SRSCD, 20 keV cascades from Caturla et al. [13] were converted into a list of initial defects for each cascade. These were then implanted into the volume elements in the simulation with a rate given by the dpa rate and the number of defects in the cascade, according to the equation in Table 1. Since the entire cascade was implanted at the same time into a single volume element, and SRSCD assumes that defects are homogeneously distributed within a volume element, the size of the volume elements used determines the local concentration of defects in a cascade. Therefore, the spatial resolution of this method is necessary because the volume element size must match approximately the size of the cascade to provide the correct initial concentration of defects.

The effect of changing the size of the volume element on the profile of vacancy cluster concentrations is shown in Fig. 3. For large meshes, the size of a volume element is much larger than the size of a cascade and the simulation produces mesh-independent results that do not match the results of OKMC. As the mesh gets smaller, the initial defect concentration increases dramatically, changing the initial clustering and annihilation rates for the defects in a given cascade. The optimal mesh size for this simulation was found to be approximately 10 nm, which is similar to the size of a 20 keV cascade. It is therefore important to note that implanting cascades in this way does not allow for mesh convergence, as only a specific mesh size best approximates the OKMC results. Future work on this topic will focus on reproducing the spatial correlations in cascades and allowing mesh convergence for smaller mesh sizes.

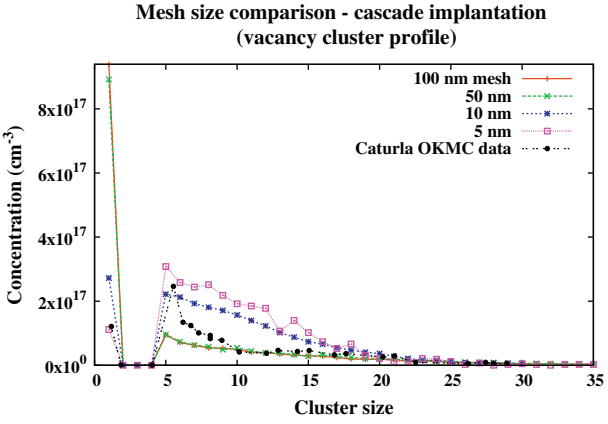

Fig. 3. Comparison of vacancy cluster profiles with varying mesh sizes at 8×10^{-4} dpa. The mesh size is critical in determining the initial concentration of defects in a cascade, and thus the mesh must match the cascade size to produce qualitatively correct results.

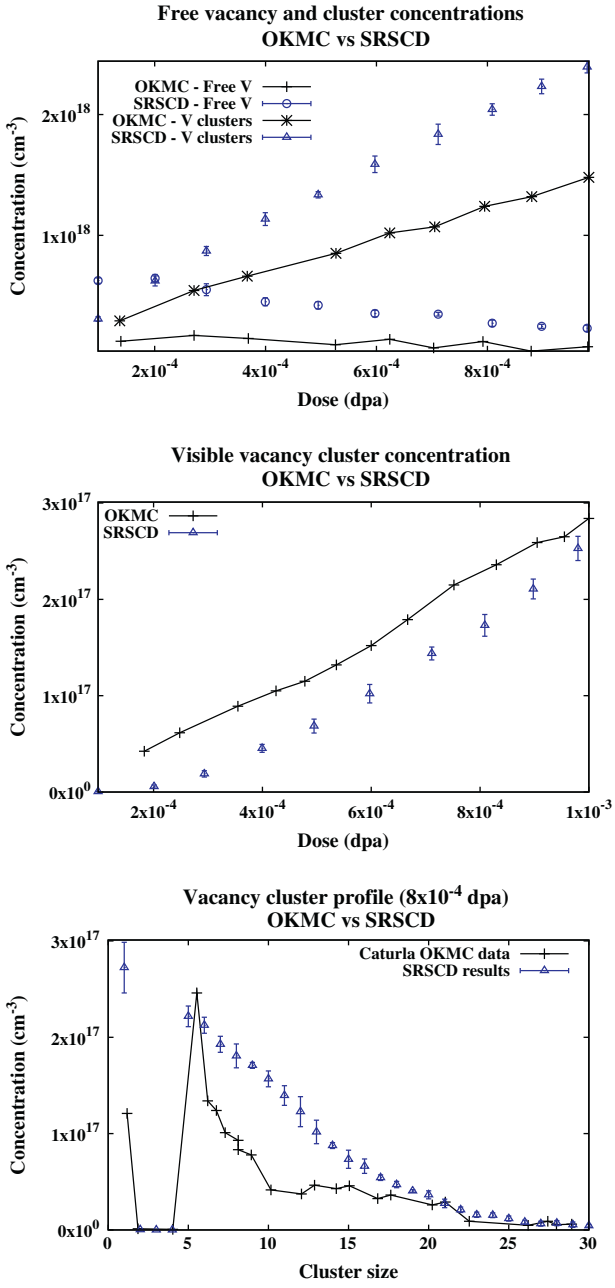

Fig. 4. SRSCD results compared to the OKMC results of Caturla et al. [13] for 20 keV cascades implanted in Cu at a dpa rate of 10^{-4} dpa/s. The qualitative results match the results of OKMC.

Simulated cascade implantation in Cu was carried out using the parameters listed in Table 3. Vacancy and cluster populations were found as a function of dpa. The results of SRSCD and the comparison to the data of Caturla et al. [13] are shown in Fig. 4. The quantitative results of this simulation differ from those of Caturla, but the qualitative trends match. The vacancy cluster concentration increases linearly with dpa, the single vacancy concentration reaches an early saturation and decreases slowly and the concentration of visible clusters also increases linearly with dpa. The vacancy cluster population profile also qualitatively matches the results of

Caturla et al., although the concentration of small vacancy clusters of size <10 differs from the results of Caturla.

The differences between the results of this model and the OKMC simulation are due to the spatial correlations that exist in 20 keV cascades in Cu that cannot be included in such a model. Specifically, Cu cascades have the property that a core region of vacancy clusters is surrounded by interstitials [41]. This model cannot simulate this type of spatial correlation, and thus some information about the initial annealing of Cu cascades may be lost. However, the results obtained here match the results of OKMC more closely than any results that can be obtained by traditional rate theory or non-spatially resolved stochastic cluster dynamics. Both the stochastic nature and the spatial resolution of this simulation allow it to reproduce many aspects of this much more computationally intensive OKMC simulation.

5. Helium desorption from Fe thin foils

5.1. Comparison of SRSCD to experiment

In order to further demonstrate the capabilities of SRSCD, the annealing of iron foils implanted with helium was simulated. This has been carried out both by experiment [25] and spatially resolved rate theory developed by Ortiz et al. [15]. In this experiment, three iron foils varying in width from 2.5 μm to 20.6 μm are implanted with helium and annealed. The material parameters for the simulation are given in Table 4.

To simulate the experimental conditions, Ortiz et al. first implanted helium, vacancies, and self-interstitials homogeneously in the material to the concentrations listed in Table 4, with 200 Frenkel pairs per helium atom introduced. The system was then allowed to reach steady-state at 300 K and subsequently annealed at high temperature. The boundaries of the iron foil were treated as free surfaces (infinite sinks for all mobile point defects) and the amount of helium released from the system as a function of time was tracked.

In the rate theory simulation by Ortiz et al. [15], the mobile species were limited to He, single vacancies, single interstitials, and 2-interstitial clusters. It is important to note that the rate equations used by the authors differ from the rate equations presented here, and can be found in [14]. Using rate theory, Ortiz et al. were able to achieve good agreement between simulation results and experiment, assuming some modified energies due to the effect of impurities in the material.

In the SRSCD simulation, the same material parameters are used, but all species which have been found to be mobile in iron are allowed to migrate. In addition, HeV and HeV_3 clusters have been studied in Nb [17] but do not have migration data available in Fe. For this simulation the migration values from Nb are used for HeV and HeV_3, but since these defects have relatively high migration energy the impact of their migration on the simulation results is negligible. The migration and binding energies of all cluster types used in this simulation are given in Table 5.

In order to include helium in the rate equations presented above, HeV clusters are assumed to be spherical with radius given by the number of vacancies in the cluster. Helium clusters are also assumed to be spherical, but the population of interstitial helium clusters is never significant. Thus reaction rates for He + HeV, V + HeV, HeV + HeV, and SIA + HeV (with the number of V greater or equal to the number of SIA) are found using the same methods as described above.

The binding of helium to single interstitials and self-interstitial clusters is a problem that has not been fully addressed in the literature. Marian and Bulatov [19] and Becquart and Domain [46] have studied defect evolution including He-SIA cluster formation, while the work of others such as Ortiz et al. [15] neglects this effect. In general, the availability of parameters governing the behavior of He-SIA clusters is low. Therefore, this simulation was carried out using only He-V clustering. In order to test the significance of this choice, identical helium desorption simulations were performed using the He-SIA parameters reported by Marian et al., assuming that He-SIA clusters are stable and immobile. Although a large number of He-SIA clusters appeared at the beginning of the annealing stage of the simulation, the change in the overall desorption results was minor. In addition, the physical mechanism of helium desorption does not change in this case. A larger study of the effect of He-SIA binding on defect accumulation in metals, with an improved set of parameters such as binding and migration energies of these defects, is warranted but outside the scope of this work.

Table 4
Material parameters used in experiment [25] and rate theory [15] studies of helium desorption from Fe foils.

Anneal temp (K)	He concentration (ppm)	Sample thickness (μm)
559	1.39	2.5
577	0.013	20.6
667	0.109	2.6

In agreement with the results of Soneda and Diaz de la Rubia [11], self-interstitial clusters of size 2 and 3 are assumed to migrate with mixed 1D–3D character, and their reaction rates for combining with other defects are calculated using the sink strength from Eq. (20). Although the frequency for direction changes is taken from the work of Soneda, in order to keep the parameter set as consistent as possible, the interstitial migration energies used are the same as those used by Marian and Bulatov [19]. These vary significantly from the migration energies for small interstitial clusters found by Soneda. However, when the simulation was repeated with the migration energies of Soneda for small interstitial clusters, the results did not change significantly. In addition, allowing only 3D migration for small interstitial clusters also produced similar results, although the migration energy of single vacancies had to be adjusted to 0.68 eV to achieve agreement with experimental results. This value is well within the range of values reported for the migration of a single vacancy in Fe [11,19]. It is therefore expected that the mixed 3D–1D migration behavior of small interstitial clusters does not have a major impact on the results of this study.

The system is evolved for 1 s at 300 K and subsequently annealed for 2×10^4 s at the higher temperature, with the boundaries of the system free surfaces for the entire simulation. The boundary conditions of the system during the low-temperature annealing part of the simulation were shown to not strongly impact the results of the simulation. The amount of helium released from the system and the types of helium clusters that leave the system are recorded.

The results provided by SRSCD differ from the experimental results given the parameters listed in Table 5. Fig. 5 shows helium desorption for the 559 K sample using SRSCD compared to experiment. Although the qualitative results match, the model predicts significantly more helium release than was measured in experiment or simulated in the rate theory model of Ortiz et al. [15].

Assuming that the material has some impurity content, interstitial clusters could be trapped and become immobile when interacting with impurity atoms [47]. In the work of Ortiz et al. [15], the migration energy of vacancies was used as a fitting parameter in order for the rate theory results to match experiment. This variation of vacancy migration energy is explained by Ortiz to be the result of the presence of impurities in the iron foil. Therefore, in this simulation, the mean free path for interstitial clusters to become immobile was varied to fit the simulation results to experimental

Table 5
Migration and binding parameters used in spatially resolved stochastic rate theory simulation of Helium desorption from Fe foil. The diffusion of HeV and HeV_3 clusters are taken from the values found for Nb, which is assumed to be similar to the behavior of Fe. For the binding energy of vacancies to large He_mV_n clusters, the He was not taken into account. A functional form for this binding energy exists [43] but does not apply to clusters where $m \ll n$. Most large HeV clusters in this simulation are of this type.

Migration parameters	$D = D_0 e^{-\frac{E_m}{k_b T}}$	
Single vacancy	E_m = 0.6 eV, $D_0 = 7.9 \times 10^{11}$ nm^2/s	[19]
2-v cluster	E_m = 0.66 eV, D_0 = 3.5×10^{10} nm^2/s	[19]
Larger v clusters	(immobile)	
Single interstitial	E_m = 0.25 eV, D_0 = 1.3×10^{10} nm^2/s	[19]
2-i Cluster	E_m = 0.36 eV, D_0 = 3.516×10^{12} nm^2/s	[19]
3-i Cluster	E_m = 0.14 eV, D_0 = 1.21×10^{11} nm^2/s	[19]
4-i Cluster	E_m = 0.15 eV, D_0 = 1.32×10^{11} nm^2/s	[19]
n-i Cluster	$D_i(n) = \frac{8.98 \times 10^{11}}{n^{-61}} e^{-\frac{.06 + .07(n^{-1.3})}{k_b T}}$ nm^2/s	[42]
Single-He	E_m = 0.077 eV, $D_0 = 5 \times 10^{11}$ nm^2/s	[43]
2-He cluster	E_m = 0.055 eV, $D_0 = 3 \times 10^{10}$ nm^2/s	[43]
HeV	E_m = 2.57 eV, $D_0 = 1.15 \times 10^{12}$ nm^2/s	[17] (value for Nb)
HeV_2	E_m = 0.27 eV, D_0 = 4.1×10^{10} nm^2/s	[44]
HeV_3	E_m = 1.42 eV, D_0 = 1.15×10^{12} nm^2/s	[17] (value for Nb)
He_2V	E_m = 0.33 eV, D_0 = 1.16×10^{11} nm^2/s	[43]
He_3V	E_m = 0.31 eV, $D_0 = 2 \times 10^{10}$ nm^2/s	[43]
He_4V	E_m = 0.28 eV, $D_0 = 2.36 \times 10^{9}$ nm^2/s	[43]
He_2V_3	E_m = 0.55 eV, D_0 = 7.82×10^{9} nm^2/s	[43]
1D–3D Direction change	$v = v_0 e^{-\frac{E_v}{k_b T}}$	
2-i Cluster	E_v = 0.088 eV, v_0 = 2.86×10^{11} s^{-1}	[11]
3-i Cluster	E_v = 0.271 eV, v_0 = 4.54×10^{11} s^{-1}	[11]
Binding energies		
Small clusters ($n \leqslant 4$)	E_b taken from Ortiz	[15]
Vacancy clusters	$E_b^v(n) = 2.07 - 3.01(n^{2/3} - (n-1)^{2/3})$	[45]
Interstitial clusters	$E_b^i(n) = 3.77 - 5.05(n^{2/3} - (n-1)^{2/3})$	[45]
He_mV_n (He binding)	$E_b^{He} = 2.2 - 1.55 \log(\frac{m}{n}) - .53 \log(\frac{m}{n})^2$	[43]
He_mV_n (V binding)	$E_b^v(n) = 2.07 - 3.01(n^{2/3} - (n-1)^{2/3})$	(Same as v clusters)

results. The simulation results were shown to depend only weakly on the actual value of the mean free path chosen and thus an optimal value of mean free path was not found. Nonetheless, the results of the simulation using this method match the experiment more closely.

It is interesting to note that if, instead of the mean free path described above, interstitial diffusion is simply eliminated for all clusters greater than size 2 in SRSCD, the results are almost identical to the use of a mean free path for interstitial cluster migration. Thus the approach of Ortiz et al., which only considers single SIAs and 2-interstitial clusters as mobile, treats interstitial migration in much the same way as this simulation. This is due to the fact that one-dimensionally migrating SIA clusters have a low cross-section for interacting with other defects and are therefore likely to reach the end of their mean free path and become sessile before interacting with other defects. Therefore the main difference between the models is the mobility of small He_mV_n clusters.

The results of the SRSCD simulation compared to experiment are shown in Fig. 6. It should be noted that SRSCD necessarily depends on a large number of binding and migration energies and prefactors, some of which are not agreed upon in the literature. The simulation results are most sensitive to binding and migration energies of small clusters such as V_2 and HeV_2. Changing any of these parameters changes the quantitative results of the simulation while (generally) keeping the qualitative results the same.

5.2. He desorption through He_mV_n cluster migration

The mechanism for helium desorption from iron foils during annealing was studied in these simulations. In the rate theory simulations of Ortiz et al. [15], He_mV_n clusters are not mobile. Helium desorption therefore occurs either by substitutional replacement by interstitials SIA + HeV → He, which leaves a mobile interstitial

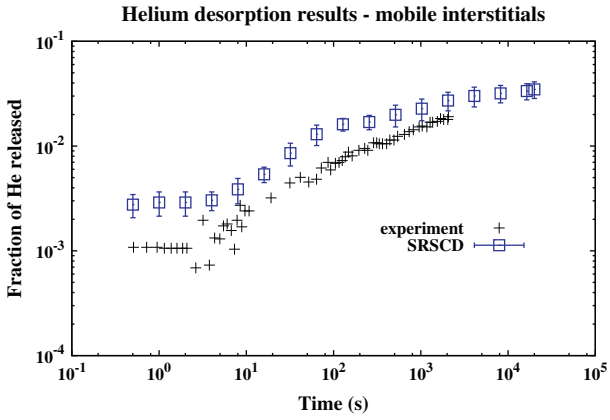

Fig. 5. % He released, 559 K anneanling. Interstitial clusters are assumed to be mobile until interacting with a second interstitial cluster, at which point they form a junction and become immobile. These results do not match the experimental results of Vassen et al. [25].

helium atom behind, or by He dissociation from HeV clusters. In either case, only mobile He interstitials can leave the free surface of the material. By contrast, studies of He_mV_n migration have shown that small clusters are in fact mobile [17,43,44,48]. Helium release from the free surfaces of a thin Fe foil through He_mV_n cluster migration is a problem particularly well-suited to SRSCD, due to the size and timescale of the system and the number of mobile species involved. By allowing small He_mV_n clusters to migrate, new regimes during which the dominant mechanism of helium desorption changes can be found using SRSCD.

To study helium release from the free surface of the foil, every instance of helium leaving the system through the free surface

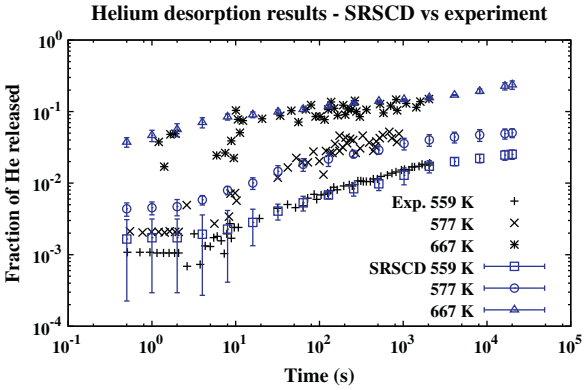

Fig. 6. Fraction of He released for experimental parameters given in Table 4.

was recorded, along with the type of defect that carried the helium out and the simulated time. The simulated annealing time was then divided into intervals representing an order of magnitude increase in annealing time. The rate of helium desorption per cm^2 of surface area for each of the three main mobile defects containing helium (interstitial He, HeV_2, He_2V_3) is then plotted for each interval. The results of this analysis are shown in Fig. 7.

The mechanism for He release from the free surface of iron foils in this simulation is dependent on both temperature and time. In all simulations, HeV_2 clusters dominate initial He release from the system. Mobile HeV_2 clusters are created first as vacancies combine with HeV clusters at early times (before 10^{-3} s at 559 K) and then as HeV_3 clusters release vacancies (up to tens of seconds at 559 K). Interstitial helium is very unlikely to reach the free surface before interacting and combining with vacancy clusters, preventing the release of interstitial helium at the free surfaces early in the simulation.

As time evolves and average cluster sizes increase, the number of HeV_3 defects present in the system decreases and the creation of HeV_2 becomes less common. At this point, the presence of He_mV_n clusters with $m > n$ becomes likely enough that dissociation of helium directly from these defects causes interstitial helium to be once again present in the material. This helium diffuses out of the material more easily than before, because the total defect density is less and interstitial helium is more likely to reach the free surface before interacting with a vacancy or He_mV_n cluster. The intermediate presence of He_2V_3 clusters comes about in a similar manner to HeV_2, as the timescale becomes longer and more clustering and dissociation reactions become feasible. The mechanism and timescale of helium release varies from sample to sample due to the differences in initial defect density and temperature of annealing. In the 667 K simulations, a small number of He_2V clusters also dissociate from the free surface near the end of the simulation.

The migration and binding energies of small HeV clusters used in this simulation likely vary from the actual values somewhat. This is due to the fact that values for migration in Nb were used in place of Fe for HeV and HeV_3 clusters, and due to the fact that other cluster types not allowed to migrate here may be mobile (HeV_4, for example). Because the rate of He desorption is very dependent on the energetics of small HeV and V clusters, the qualitative results of this simulation should be emphasized over the quantitative results. As the parameters describing the behavior of helium, vacancies, and interstitials improve, the results of such simulations should match reality more closely.

In the analysis of Ortiz et al. [15], the initial He release is caused by self-interstitial clusters dissociating at the annealing temperature and creating interstitial He through substitution replacement

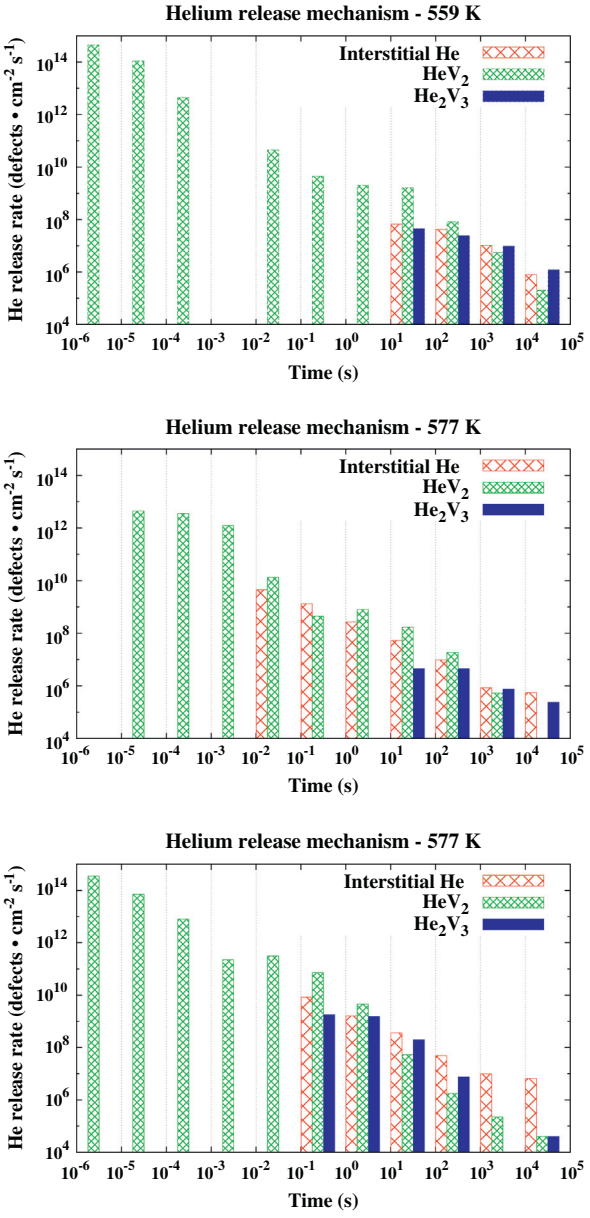

Fig. 7. Release rates for time intervals of annealing of interstitial He, HeV_2, and He_2V_3 from iron foils for the three samples listed above. As time evolves, the mechanism of helium release shifts from HeV_2 to interstitial He and He_2V_3.

reactions with HeV clusters. The subsequent, long-time annealing behavior is then caused by He dissociation from He_mV_n clusters. However, their rate theory simulation does not account for mobility of small HeV clusters and therefore may not capture some of the effects described here.

6. Conclusions

A spatially resolved stochastic cluster dynamics (SRSCD) method has been developed in order to simulate the evolution of radiation damage in spatially non-homogeneous systems. This method has the advantages over OKMC and MFRT methods that simulations can be carried out in minutes to hours, length scales on the order of tens of microns can be simulated, and arbitrary species and mobile defects can be included in the simulation without exponentially increasing computation time.

SRSCD is first used to reproduce both spatially homogeneous and single-crystal thin film implantation of Frenkel pairs, comparing results in both cases to those of traditional rate theory using the parameters of Stoller et al. [10]. Results are found to match those of rate theory, and the amount of computation required in this simulation is significantly lower using SRSCD.

Implantation of 20 keV cascades in Cu is also simulated using SRSCD and compared to the results of OKMC [13]. The qualitative results of the simulation match, but quantitative differences due to the effects of the spatial correlations of defects within individual cascades are found. The spatial resolution of SRSCD is found to be necessary to provide reasonable agreement with OKMC. The volume element size must match the approximate size of the implanted cascades for initial clustering and recombination rates to be correct. The best method for representing cascade damage in a model such as this is still an open question that will be investigated in future work.

The strength of SRSCD is demonstrated in simulations of helium desorption from thin foils. These simulations are compared to experiment and rate theory simulations [15,25]. Due to the ability of SRSCD to include multiple mobile He_mV_n clusters, this simulation is able to find new regimes during which helium desorption is dominated by different mechanisms. Early helium desorption is dominated by HeV_2 migration, and later desorption consists of interstitial helium dissociation from clusters and migration out of the material.

Acknowledgements

The authors gratefully acknowledge support from European Union, Project RADINTERFACES. The authors thank I. Martin-Bragado and L. Agudo for their discussions and assistance on this work. The authors thank C. Ortiz and M.J. Caturla for their correspondence. A. Dunn would like to thank M. McPhie for discussions on this work. E. Martinez gratefully acknowledges support from the Center for Materials at Irradiation and Mechanical Extremes, an Energy Frontier Research Center funded by the US Department of Energy (Award Number 2008LANL1026) at Los Alamos National Laboratory.

References

[1] M. Demkowicz, P. Bellon, B. Wirth, MRS Bulletin 35 (2010) 941–1056.
[2] S. Ukai, M. Fujiwara, Journal of Nuclear Materials 307–311 (2002) 749–757.
[3] A. Misra, M. Demkowicz, X. Zhang, R. Hoagland, JOM Journal of the Minerals, Metals, and Materials Society 59 (2007) 62–65.
[4] M. Demkowicz, Y. Wang, R. Hoagland, O. Anderoglu, Nuclear Instruments and Methods in Physics Research B 261 (2007) 524–528.
[5] S. Zinkle, B. Singh, Journal of Nuclear Materials 283–287 (2000) 306–312.
[6] A. Ryazanov, D. Braski, H. Schroeder, H. Trinkaus, H. Ullmaier, Journal of Nuclear Materials 233 (1996) 1076–1079.
[7] H. Heinisch, F. Gao, R. Kurtz, E. Le, Journal of Nuclear Materials 351 (2006) 141–148.
[8] H. Heinisch, F. Gao, R. Kurtz, Journal of Nuclear Materials 367–370 (2007) 311–315.
[9] A.D. Brailsford, R. Bullough, Mathematical and Physical Sciences 302 (1981) 87–137.
[10] R. Stoller, S. Golubov, C. Domain, C. Becquart, Journal of Nuclear Materials 382 (2008) 77–90.
[11] N. Soneda, T. Diaz de la Rubia, Philosophical Magazine A 78 (1998) 995–1019.
[12] C. Domain, C. Becquart, L. Malerba, Journal of Nuclear Materials 335 (2004) 121–145.
[13] M. Caturla, N. Soneda, E. Alonso, B. Wirth, T. Diaz de la Rubia, J. Perlado, Journal of Nuclear Materials 276 (2000) 13–21.
[14] C.J. Ortiz, M.J. Caturla, Physical Review B 75 (2007) 184101.
[15] C.J. Ortiz, M.J. Caturla, C.C. Fu, F. Willaime, Physical Review B 75 (2007) 100102.
[16] Y. Li, W. Zhou, L. Huang, Z. Zeng, X. Jub, Journal of Nuclear Materials 431 (2012) 26–32.
[17] A. Dunn, M. McPhie, L. Capolungo, E. Martinez, M. Cherkaoui, Journal of Nuclear Materials 435 (2013) 141–152.
[18] Q. Xu, N. Yoshida, T. Yoshiie, Journal of Nuclear Materials 367–370 (2007) 806–811.
[19] J. Marian, V.V. Bulatov, Journal of Nuclear Materials 415 (2011) 84–85.
[20] K. Tapasa, A. Barashev, D. Bacon, Y. Osetsky, Acta Materialia 55 (2007) 1–11.
[21] G. Odette, G. Lucas, JOM 53 (2001) 18–22.
[22] L. Wang, R. Dodd, G. Kulcinski, Journal of Nuclear Materials 141–143 (1986) 713–717.
[23] T. Tanaka, K. Oka, S. Ohnuki, S. Yamashita, T. Suda, S. Watanabe, E. Wakai, Journal of Nuclear Materials 329–333 (2004) 294–298.
[24] D.T. Gillespie, Journal of Computational Physics 22 (1976) 403–434.
[25] R. Vassen, H. Trinkaus, P. Jung, Physical Review B 44 (1991) 4206–4213.
[26] J.L. Katz, H. Wiedersich, Journal of Chemical Physics 55 (1971) 1414–1425.
[27] S.I. Golubov, M. Ovcharenko, A.V. Barashev, B.N. Singh, Philosophical Magazine A 81 (2001) 643–658.
[28] N.V. Doan, G. Martin, Physical Review B 67 (2003) 134107.
[29] S.L. Dudarev, A.A. Semenov, C.H. Woo, Physical Review B 67 (2003) 094103.
[30] Y. Osetsky, D. Bacon, B. Singh, B. Wirth, Journal of Nuclear Materials 307–311 (2002) 852–861.
[31] W. Schilling, K. Schroeder, H. Wollenberger, Physica Status Solidi 38 (1970) 245–257.
[32] H. Trinkaus, B. Singh, S. Golubov, Journal of Nuclear Materials 283–287 (2000) 89–98.
[33] H. Trinkaus, H.L. Heinisch, A.V. Barashev, S.I. Golubov, B.N. Singh, Physical Review B 66 (2002) 060105.
[34] M.J. Demkowicz, D. Bhattacharyya, I. Usov, Y.Q. Wang, M. Nastasi, A. Misra, Applied Physics Letters 97 (2010) 161903.
[35] K. Hattar, M. Demkowicz, A. Misra, I. Robertson, R. Hoagland, Scripta Materialia 58 (2008) 541–544.
[36] M. Zhernenkov, M.S. Jablin, A. Misra, M. Nastasi, Y. Wang, M.J. Demkowicz, J.K. Baldwin, J. Majewski, Applied Physics Letters 98 (2011) 241913.
[37] M. Sabochick, S. Yip, Journal of Physics F 18 (1988) 1689–1701.
[38] J.W. Corbett, R.B. Smith, R.M. Walker, Physical Review 114 (1959) 1460–1472.
[39] H. Schober, R. Zeller, Journal of Nuclear Materials 69–70 (1978) 341–349.
[40] Y. Osetsky, A. Serra, V. Priego, Journal of Nuclear Materials 276 (2000) 202–212.
[41] T. Diaz de la Rubia, M.W. Guinan, Physical Review Letters 66 (1991) 2766–2769.
[42] J. Marian, B.D. Wirth, R. Schaublin, G. Odette, J.M. Perlado, Journal of Nuclear Materials 323 (2003) 181–191.
[43] D. Terentyev, N. Juslin, K. Nordlund, N. Sandberg, Journal of Applied Physics 105 (2009) 103509.
[44] C.-C. Fu, F. Willaime, Physical Review B 72 (2005) 064117.
[45] C.-C. Fu, J.D. Torre, F. Willaime, J.-L. Bocquet, A. Barbu, Nature Materials 4 (2005) 68–74.
[46] C. Becquart, C. Domain, Journal of Nuclear Materials 385 (2009) 223–227.
[47] T.S. Hudson, S.L. Dudarev, A.P. Sutton, Proceedings of the Royal Society of London Series A – Mathematical, Physical, and Engineering Sciences 460 (2004) 2457–2475.
[48] V. Borodin, P. Vladimirov, Diffusion coefficients and thermal stability of small helium-vacancy clusters in iron, Journal of Nuclear Materials 362 (2007) 161–166.